

Future evolution of global land surface air temperature trend based on Coupled Model Intercomparison Project Phase 6 models

Wen Wu¹ | Fei Ji^{1,2}  | Shujuan Hu^{1,2}  | Yongli He^{1,2} | Yun Wei¹  | Zhenhao Xu^{3,4} | Haipeng Yu⁵

¹College of Atmospheric Sciences,
Lanzhou University, Lanzhou, China

²Collaborative Innovation Center for
Western Ecological Safety, Lanzhou
University, Lanzhou, China

³State Key Laboratory of Numerical
Modeling for Atmospheric Sciences and
Geophysical Fluid Dynamics, Institute of
Atmospheric Physics, Chinese Academy
of Sciences, Beijing, China

⁴College of Earth and Planetary Sciences,
University of Chinese Academy of
Sciences, Beijing, China

⁵Key Laboratory of Land Surface Process
and Climate Change in Cold and Arid
Regions, Northwest Institute of Eco-
Environment and Resources, Chinese
Academy of Sciences, Lanzhou, China

Correspondence

Fei Ji and Shujuan Hu, College of
Atmospheric Sciences, Lanzhou
University, Lanzhou, China.
Email: jif@lzu.edu.cn (F.J.) and
hushuju@lzu.edu.cn (S.H.)

Funding information

National key research and development
program, Grant/Award Numbers:
2017YFC1502305, 2019YFA0607104;
National Natural Science Foundation of
China, Grant/Award Numbers: 41775069,
41875083, 41975076, 42075017, 42075029,
42175054

Abstract

In recent decades, global warming has been an indisputable fact. The increase in extreme events accompanied by the rise in temperature has huge influences on many aspects of the society and economy globally. As a result, forecasting how global temperatures will change and evolve in the future is crucial, but it is restricted by the accuracy and uncertainty of model simulations. Based on ensemble empirical mode decomposition (EEMD) method, this study first evaluates the performance of the CMIP6 models in simulating different timescale components including high-frequency components (HFC), low-frequency components (LFC), and secular trend (ST) of surface air temperature (SAT). The results show that the performance of the CMIP6 models in simulating the ST is better. Following the observation constraint method's correction of CMIP6 model simulations, we investigate the evolution characteristics of future temperature secular trends under different Shared Socioeconomic Pathway (SSP) scenarios. The results show that under SSP245 scenario, the rise of SAT first appeared in northwest and east North America and eastern Europe. The spatial distribution of evolution characteristic under the SSP585 scenario is similar to that of the SSP245 scenario but with a larger magnitude. However, more pronounced differences appear in warming rate, which shows a downward trend over time under the SSP245 scenario and an upward trend with time under the SSP585 scenario.

KEY WORDS

CMIP6, EEMD, future evolution, surface air temperature

1 | INTRODUCTION

A study by the World Meteorological Organization (WMO) shows that as of 2020, the global average annual surface temperature relative to the pre-industrial warming range is $1.2 \pm 0.1^\circ\text{C}$ (Kennedy *et al.*, 2021). This

is very close to the Paris Climate Agreement's goal of limiting warming to 1.5°C , and 2020 has become one of the three hottest years on record (Stocker *et al.*, 2014; UNFCCC, 2015; IPCC, 2022; Kennedy *et al.*, 2021). The rise in temperature is not only accompanied by the melting of sea ice, the rise in sea level, and the increase in

ocean temperature and acidity, which weaken the ocean's ability to mitigate climate change. In addition, warming has led to more and stronger extreme weather and climate events, which will have a huge impact on the global economy, agriculture, hydrology, and the safety of life and property (Ma and Xie, 2013; Huang *et al.*, 2017; Jiang *et al.*, 2020; Yao *et al.*, 2020; Ferrero *et al.*, 2021; Qin *et al.*, 2021; Rao *et al.*, 2021). Therefore, it is of great significance to study how future climate will change.

So far, climate models are our main practical tools for studying past and future climate simulations. In the historical period, studies have shown that the simulation of the previous phases of the Coupled Model Intercomparison Project (CMIP3, CMIP5, CMIP6) and reanalysis data of surface air temperature are very close (Kumar *et al.*, 2014; Chen and Sun, 2015; Chen *et al.*, 2020a). Therefore, a large number of researches on future temperature changes are carried out based on the CMIPs model ensemble mean (Ma and Xie, 2013; Tokarska *et al.*, 2020; Zhu *et al.*, 2020; Long *et al.*, 2021; Thaler *et al.*, 2021). However, the global climate model (GCM) generally has a low resolution, and the setting of the underlying surface characteristics of the specific area under study is relatively rough, resulting in differences between the model results and the observation or reanalysis data (Xie *et al.*, 2016; Li *et al.*, 2018; Liu *et al.*, 2018; Kodra *et al.*, 2020). The regional climate model (RCM) can dynamically downscale the output of GCM to obtain more detailed and reliable regional climate information. Compared with GCM, RCM can provide higher resolution and more detailed local information. Therefore, many studies on various climate indicators are based on RCM (Piani *et al.*, 2010; Shen *et al.*, 2020; Coppola *et al.*, 2021; Qin *et al.*, 2021). For future simulations, CMIP5 has provided a set of Representative Concentration Pathway (RCP) scenarios to describe the emissions of greenhouse gases, reactive gases, and aerosols, and the concentration of atmospheric components when changes in population, social economy, and land use occur in the future (Moss *et al.*, 2010; Taylor *et al.*, 2012). The Shared Socioeconomic Pathway (SSP) scenarios developed in CMIP6 are an upgrade of the four RCPs in CMIP5 and include some new emission pathways in order to facilitate scientific researchers to have more options when making future climate predictions (Eyring *et al.*, 2016; Zhao *et al.*, 2021).

In fact, whether it is GCM or RCM, there will always be differences in the model's simulation of various climate factors (Maraun *et al.*, 2017; Brient, 2020; Lu, 2020). In order to improve the credibility of the model for simulating various climate variables, various model bias correction methods have been emphasized and developed (Wenzel *et al.*, 2014; Choi *et al.*, 2016; Bowman *et al.*, 2018). They are mainly divided into two categories; one is to correct the model outputs based on statistical methods (Huang *et al.*, 2016; Yao

et al., 2020). The establishment of statistical relationships is mostly based on multiple linear regression, quantile mapping (QM) or machine learning methods, etc (Piani *et al.*, 2010; Terink *et al.*, 2010; Gu *et al.*, 2020; Liu *et al.*, 2020; Mishra *et al.*, 2020; Shen *et al.*, 2020). The other is the emergence constraints (ECs; Kwiatkowski *et al.*, 2017; Hall *et al.*, 2019; Krinner *et al.*, 2020). It aims to find the relationship between the dispersion of climate prediction in multimodels and climate observations of predictors, so as to reduce the uncertainty of model prediction (Klein and Hall, 2015; Li *et al.*, 2017; Caldwell *et al.*, 2018; Chen *et al.*, 2020b).

Generally, efforts mentioned above are made to improve the estimation of future climate change, especially for the mean state of a climate factor, such as the temperature. The mean state of a variable always contains limited information, which however can be provided by other aspects of that variable including the variability at different timescales (Qi *et al.*, 2017). Here, for surface air temperature (SAT), we tend to pay more attention to its secular trend change, which depends on the methods we used to extract the trend component. Although there are many scale separation methods, there are currently fewer applications in temperature research. Some studies only take year smooth methods to filter (Zhang *et al.*, 2021). The time series obtained by this method cannot be wholly considered as a trend change in temperature. We need a more accurate filtering scheme. The multidimensional ensemble empirical mode decomposition (MEEMD) method is proposed to solve this problem (Huang *et al.*, 1998; Wu *et al.*, 2009; Wu and Huang, 2009). Although there have been some studies that decompose the original time series based on this method, they do not reflect the essential advantage of the MEEMD method, that is, the secular trend component decomposed by the MEEMD method is nonlinear, and spatial-temporally varying, which is good at capturing the evolution characteristics of the studied variables (Ji *et al.*, 2014; Xu *et al.*, 2021). Therefore, this study selects the Phase 6 of the Coupled Model Intercomparison Project (CMIP6) models which have high skills in capturing the evolution characteristics of secular trend (ST) of SAT extracted by MEEMD. The chosen models' outputs' biases are then corrected to increase the credibility of future projections, so as to more accurately study the evolution characteristics of ST of SAT in different scenarios in the future.

2 | DATA AND METHODS

2.1 | Data

In this study, the monthly averaged SAT over global land from the Climatic Research Unit (CRU) TS v.4.05 dataset,

TABLE 1 Basic information of each mode of CMIP6 (name, modelling centres and countries)

Model name	Modelling centre and country
ACCESS-CM2	Australian Community Climate and Earth System Simulator (Australia)
ACCESS-ESM1-5	Australian Community Climate and Earth System Simulator (Australia)
BCC-CSM2-MR	Beijing Climate Center (China)
CAMS-CSM1-0	Chinese Academy of Meteorological Sciences (China)
CanESM5	Canadian Centre for Climate Modelling and Analysis (Canada)
CAS-ESM2-0	Chinese Academy of Sciences (China)
CESM2	National Center for Atmospheric Research (USA)
CESM2-WACCM	National Center for Atmospheric Research (USA)
EC-Earth3	European Centre-Earth-Consortium (Europe)
EC-Earth3-Veg	European Centre-Earth-Consortium (Europe)
FGOALS-g3	Institute of Atmospheric Physics, Chinese Academy of Sciences (China)
FIO-ESM-2-0	First Institute of Oceanography (China)
GFDL-ESM4	Geophysical Fluid Dynamics Laboratory (USA)
GISS-E2-1-G	National Aeronautics and Space Administration (USA)
GISS-E2-1-H	National Aeronautics and Space Administration (USA)
IITM-ESM	Centre for Climate Change Research, Indian Institute of Tropical Meteorology (India)
INM-CM4-8	Institute for Numerical Mathematics (Russia)
INM-CM5-0	Institute for Numerical Mathematics (Russia)
IPSL-CM6A-LR	Institute Pierre-Simon Laplace (France)
KACE-1-0-G	National Institute of Meteorological Sciences, Korea Meteorological Administration (Korea)
KIOT-ESM	Korea Institute of Ocean Science & Technology (Korea)
MCM-UA-1-0	Manabe Climate Model, University of Arizona (USA)
MIROC6	Atmosphere and Ocean Research Institute (Japan)
MPI-ESM1-2-HR	Max Planck Institute for Meteorology (Germany)
MPI-ESM1-2-LR	Max Planck Institute for Meteorology (Germany)
MRI-ESM2-0	Meteorological Research Institute (Japan)
NESM3	Nanjing University of Information Science and Technology (China)
NorESM2-LM	Norwegian Climate Centre (Norway)

provided by the University of East Anglia, is analysed. This data covers the period 1901–2020 and has a resolution of $0.5^\circ \times 0.5^\circ$ (Harris *et al.*, 2020). In addition, 28 models in CMIP6 were obtained from <https://esgf-node.llnl.gov/search/cmip6/>, and only the first set member was selected for each model (Table 1). In order to be consistent with the time span and resolution of the reanalysis data, the reanalysis data and historical outputs of the CMIP6 models are selected from 1901 to 2014, and a statistical downscale was adopted to $0.5^\circ \times 0.5^\circ$.

2.2 | Evaluation index

There are many objective quantitative evaluation methods. This study mainly evaluates the model simulation skills of

historical periods from two aspects. Spatially, the anomaly correlation coefficient (ACC) is used to evaluate the consistency of the model data anomalies and the reanalysis data anomalies. The closer the ACC is to 1, the closer the model anomalies are to the reanalysis data; the root-mean-square error (RMSE) is used to evaluate the distance between the model data and the reanalysis data. The smaller the RMSE is, the smaller the distance between the model and the reanalysis data.

In addition, the temporal correlation coefficient (TCC) is used to evaluate the time consistency between model data and the reanalysis data. The closer the TCC is to 1, the better the time consistency between the model and the reanalysis data; the Root_i (R_i) is used to value the temporal difference between the model and the reanalysis data, and the smaller R_i represents the smaller

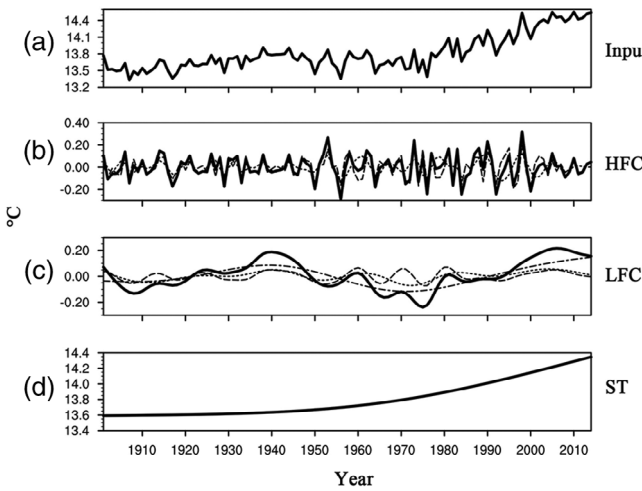


FIGURE 1 EEMD decomposition of CRU global land annual average SAT from 1901 to 2014 to get each component. (a) is the original time series of CRU global land annual average SAT from 1901 to 2014; (b) the midpoint line, the broken line represents the first two IMFs, the black solid line represents HFC in (a); (c) the midpoint line, the broken line and the dotted broken line respectively represent the last three IMFs, and the solid black line represents LFC in (a); (d) is the remainder, which represents ST in (a)

temporal difference between the value of the model data and the reanalysis.

2.3 | The multidimensional ensemble empirical mode decomposition

In this article, we take advantage of multidimensional ensemble empirical mode decomposition (MEEMD; Wu *et al.*, 2009) to depict global patterns of spatial-temporally secular evolution in SAT. This method is a temporally local and adaptive method based on ensemble empirical mode decomposition (EEMD; Huang *et al.*, 1998; Huang and Wu, 2008; Wu and Huang, 2009). EEMD is mainly used for single time series, while MEEMD is extended to multidimensional data, both of which have been widely used in climate research (Qian *et al.*, 2010; Ji *et al.*, 2014; Chen *et al.*, 2017; Xu *et al.*, 2021). Here we briefly introduce the method and the detailed procedures are available in the aforementioned studies. In EEMD, a time series $x(t)$ is decomposed into a set of oscillatory components (intrinsic mode functions, IMFs) $c_j(t)$, $j = 1, 2, \dots, n$ and a residual $R(t)$,

$$x(t) = \sum_{j=1}^n c_j(t) + R(t). \quad (1)$$

In this paper, the white noise with variance $\sigma = 0.2$ relative to the variance of the raw data, and ensemble

members are 400. The number of IMFs obtained by EEMD is determined by the length of the time series we studied. The selection criteria are shown in Equation (2), where N represents the number of eigenmodes we finally got, m represents the length of the time series, and fix represents a rounding function,

$$N = fix[\log_2(m) - 1]. \quad (2)$$

Since the data we studied is from 1901 to 2014, we will get five IMFs representing signals with different timescales including interannual, interdecadal, and multidecadal variabilities, and one remainder representing the ST. Then, it is not difficult to find that imf1 (the midpoint line in Figure 1b) and imf2 (the broken line in Figure 1b) are both 2–7 year scale components, add them to get the high-frequency components (HFC) component of SAT. Also, imf3 (the midpoint line in Figure 1c), imf4 (the broken line in Figure 1c), and imf5 (the dotted broken line in Figure 1c) are the 15–40 year scale components, add them to get the low-frequency components (LFC) component of SAT. Figure 1d is the remaining $R(t)$ after EEMD, which represents the ST of SAT in the historical period. After extending EEMD to multidimensional spatial-temporal SAT data, we pieced together $R(t)$ s from all available grids to form entire pictures of EEMD trends at the centennial timescale. This is the natural advantage of the MEEMD method, which will provide much more detailed images of how global SAT has evolved in a centennial timescale, compared with the traditional linear method.

3 | RESULTS

3.1 | Model evaluation

Most commonly, researchers quantify model performance by comparing the observations with model simulations, which mainly focus on the mean state of a climate variable and ignore different models' capacity on simulating climate variability at different timescales. Here, we extracted three components (HFC, LFC, and ST) of SAT by EEMD and then evaluated model performances for the different timescale components, respectively. A Taylor diagram is utilized to facilitate this process, which is shown by ACC and RMSE in Figure 2a, b. Taking the average ACC and RMSE of 28 models as the dividing standard, four sub-regions are obtained. According to the definition of ACC and RMSE, the region in the fan-shaped area below the intersection is selected as the model with high-simulation skills in terms of spatial consistency. From Figure 2a, it can be found that the

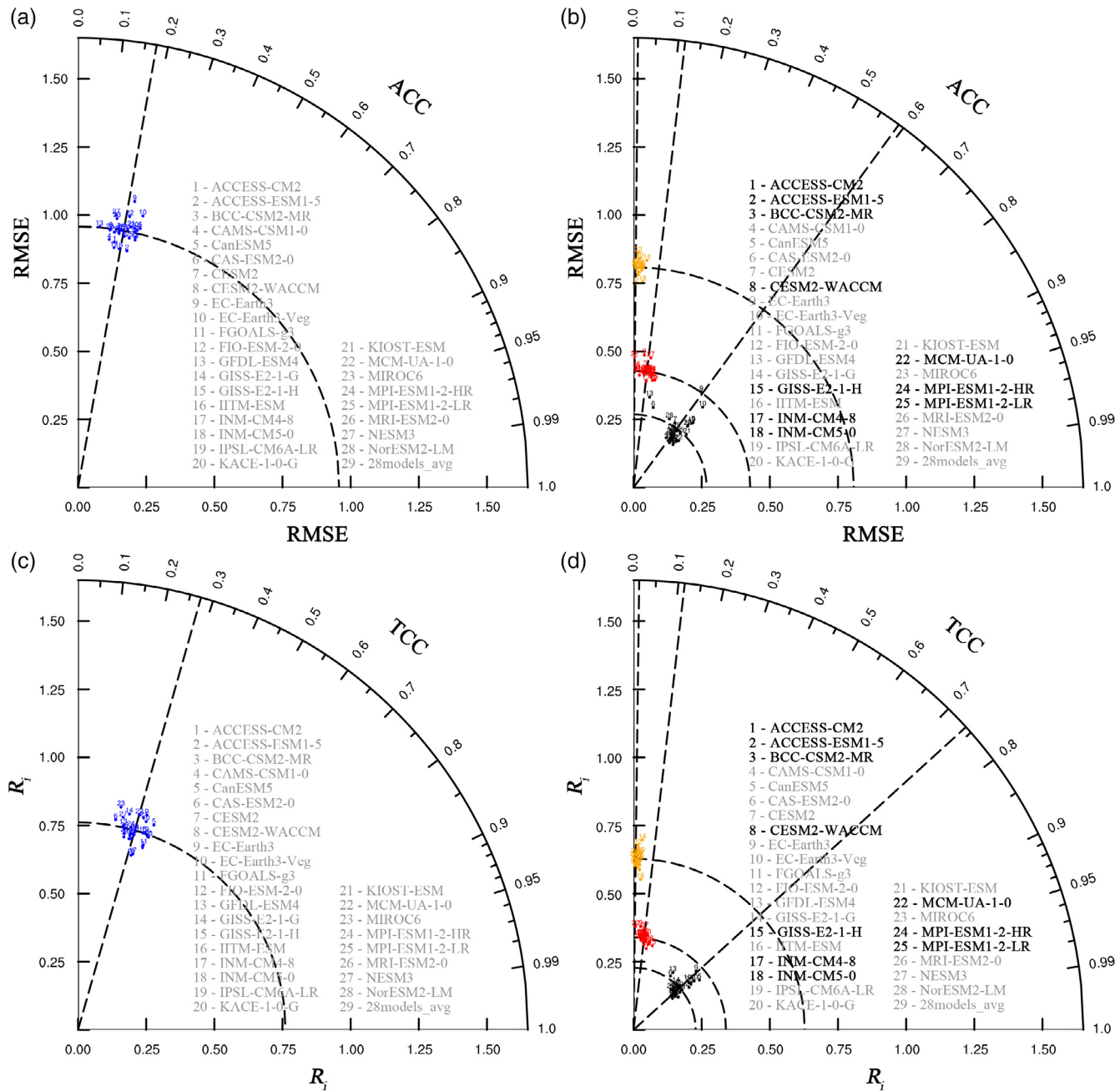


FIGURE 2 1901–2014 (a) overall, (b) HFC (orange), LFC (red) and ST (black) 114-year average ACC and RMSE between the SAT of CRU and 28 CMIP6 models. The rectangular coordinates represent RMSE, and the polar coordinates represent ACC. (c) Overall, (d) HFC (orange), LFC (red) and ST (black) global zonal weighted average of TCC and R_i . The rectangular coordinates represent R_i , and the polar coordinates represent TCC. The dotted line represents the average of evaluation index of the 28 models. The dark and bold legend in the figure indicates models which have high simulation skills in both time and space of ST [Colour figure can be viewed at wileyonlinelibrary.com]

distributions of ACC and RMSE among the models are relatively concentrated, which means intermodels' differences of the SAT are relatively small. The average ACC and RMSE of the 28 models are 0.18 and 0.96, respectively. It can be seen that the model itself is not good for the overall spatial simulation results of the SAT in the historical period. Only five models with high overall

simulation skills are determined, namely: ACCESS-ESM1-5, CESM2-WACCM, FGOALS-g3, GISS-E2-1-H, and MPI-ESM1-2-LR. After specific analysis of the ACC and RMSE of each year, it is found that the years with poor performance of each model are concentrated from 1950 to 1970, and the ACC of some models are even showed a negative value during this period.

After decomposition using the EEMD method, the model's simulation skills for each component from high to low are ST, LFC, and HFC (Figure 2b). There are six models show high simulation skills of the HFC, and the average ACC and RMSE of all models are 0.0099 and 0.81. There are 11 models with high simulation skills in the LFC. The aggregate average ACC and RMSE of all models are 0.12 and 0.43, which is better than the simulation result of the HFC. The simulation result of the ST shows that there are 13 high-skilled models, and the average ACC and RMSE are 0.59 and 0.27, which are not only better than the other two components in the historical period simulation, but also significantly better than the overall model simulation. The result shows that the model has a poor ability to capture and simulate high-frequency signals. Only one model named ACCESS-ESM1-5 has a high skill in the simulation of these three components at the same time.

In terms of time consistency, we calculate the TCC and R_i of the 28 CMIP6 models whole and the three components with the reanalysis data, and draw the Taylor diagram based on the global zonal weighted average which are shown in Figure 2c,d. From Figure 2c, the simulations of the overall time evolution of the models are relatively consistent. The average TCC and R_i of the 28 models are 0.27 and 0.76, respectively. In the historical period, models are consistent in time simulation is better than spatial consistency compared with Figure 2a, and there are nine models with high overall simulation skills, namely ACCESS-ESM1-5, CESM2, FGOALS-g3, FIO-ESM-2-0, GISS-E2-1-H, INM-CM4-8, INM-CM5-0, KACE-1-0-G, and MPI-ESM1-2-LR. There are four models with high overall simulation skills in time and space, namely ACCESS-ESM1-5, FGOALS-g3, GISS-E2-1-H, and MPI-ESM1-2-LR.

Figure 2d has shown that the simulation techniques in time consistency of each component are consistent with the results of ACC and RMSE, the ST is higher than the LFC and the HFC. There are seven models with high simulation skills for the HFC, and the average TCC and R_i of all models are 0.013 and 0.63, respectively. There are 12 models with high simulation skills for the LFC, and the average TCC and R_i values of all models are 0.11 and 0.34, respectively. There are 10 models with high ST simulation skills, and the average TCC and R_i of the 28 models are 0.74 and 0.23, respectively. Obviously, the model has the best simulation results for the ST, and the simulation skills of model and CRU in terms of time consistency are generally higher than the spatial consistency. The models with high simulation skills in all components are ACCESS-ESM1-5 and INM-CM5-0. These two models also have high simulation skills in the overall assessment of time consistency. The comprehensive evaluation results of both time and space show that only ACCESS-ESM1-5 has high

simulation skills in both the overall and the three components.

3.2 | Bias correction

It can be found from Figure 2 that in terms of space and time evaluation, most models fail to pass the significance test for the simulation results of the HFC and LFC in historical periods. According to the evaluation results, a total of 10 models with high simulating skills of ST in both space and time were selected, namely ACCESS-CM2, ACCESS-ESM1-5, BCC-CSM2-MR, CESM2-WACCM, GISS-E2-1-H, INM-CM4-8, INM-CM5-0, MCM-UA-1-0, MPI-ESM1-2-HR, and MPI-ESM1-2-LR, find the ST of these model ensemble mean (CMIP6-EM), and compare them with the ST of the CRU (Figure 3, left and middle columns). It is found that the CMIP6-EM has a high simulation skill in the evolution of ST. Before 1970, the model's simulation of the spatial modalities in the evolution of ST of SAT was poor, mainly manifested in that the warming first appeared in the high latitudes of the Eurasian continent and the eastern parts of North America in the reanalysis data, while the CMIP6-EM simulation results showed that warming first appeared in the middle latitude regions of the Eurasian continent and the high-latitude regions of North America. Also, CMIP6-EM incorrectly simulated the cooling trend in the low-latitude regions of Africa and South America as a warming trend. After 1970, the simulation skills of the model have improved, which is mainly manifested in the capture of temperature evolution modes in the middle and high latitudes of the Northern Hemisphere. However, in general, the consistency of the evolution of ST between CMIP6-EM and CRU is poor.

Therefore, we correct CMIP6-EM by following the process from Huang and Yu because of the significant correction effect for low-frequency signals (Huang *et al.*, 2016; Huang *et al.*, 2017; Wei *et al.*, 2021; Yu *et al.*, 2022). The CRU original temperature field and the CMIP6-EM original temperature field in the historical period were decomposed by the empirical orthogonal function (EOF) method, and the time coefficients of the first 18 modes of the CRU original temperature field and the CMIP6-EM original temperature field were selected in combination with the variance of each mode obtained by the decomposition to establish a multiple linear regression relationship, which is used to correct CMIP6-EM time coefficients. Then, the corrected time coefficients of CMIP6-EM are combined with the spatial pattern of the CRU original temperature field to obtain the corrected CMIP6-EM temperature field (CMIP6-EM_{cor}). Comparing the CRU with CMIP6-EM_{cor} (right column in Figure 3), it is found that CMIP6-EM_{cor} has corrected incorrect simulation of CMIP6-EM before 1970. After 1970,

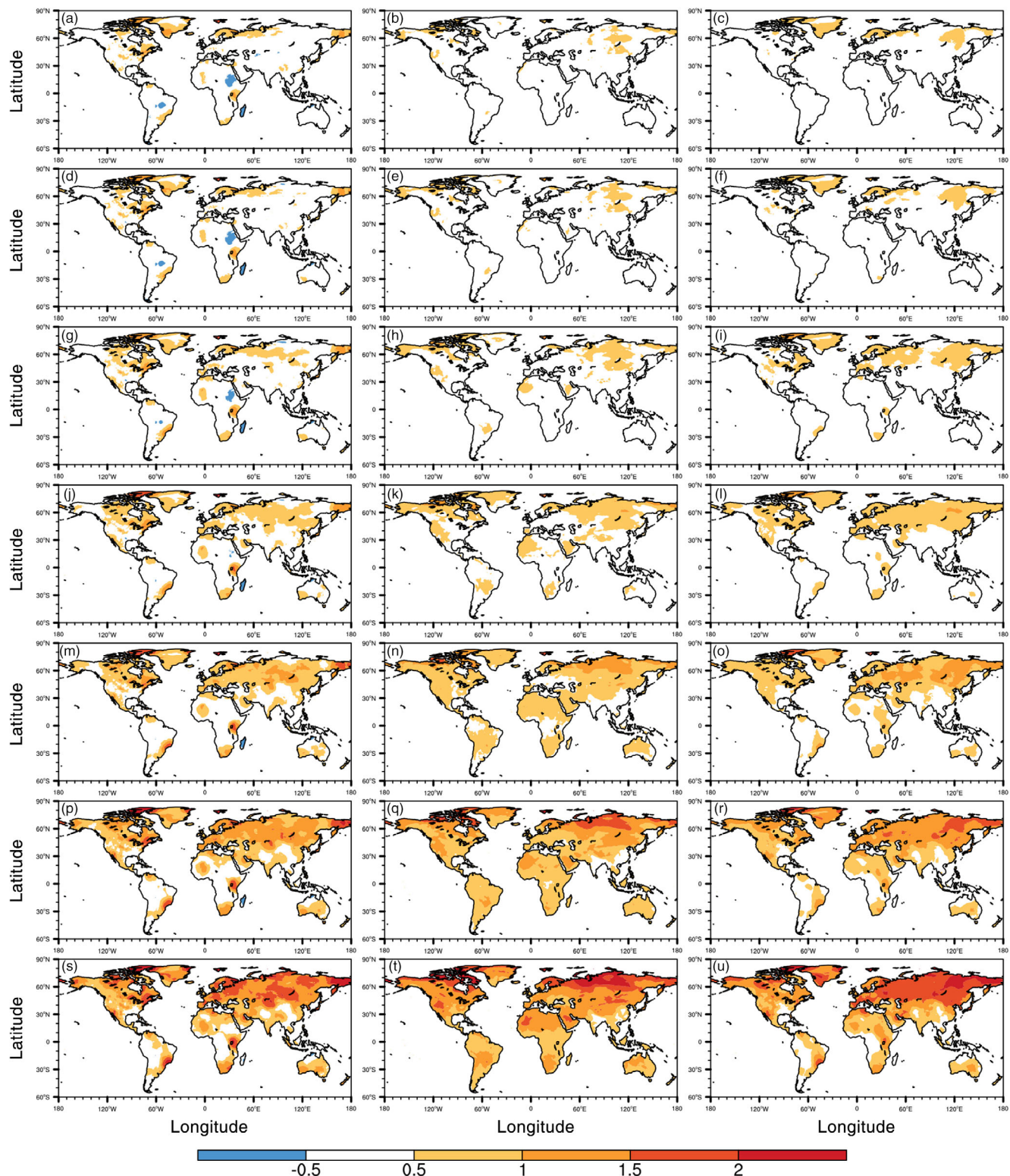


FIGURE 3 The evolution of ST in CRU (left column), CMIP6-EM (middle column) and CMIP6-EM_{cor} (right column). (a–c) represents evolution of 1950 relative to 1901; (d–f) represents 1960; (g–i) represents 1970; (j–l) represents 1980; (m, n, o) represents 1990; (p–r) represents 2000; (s–u) represents 2010 [Colour figure can be viewed at wileyonlinelibrary.com]

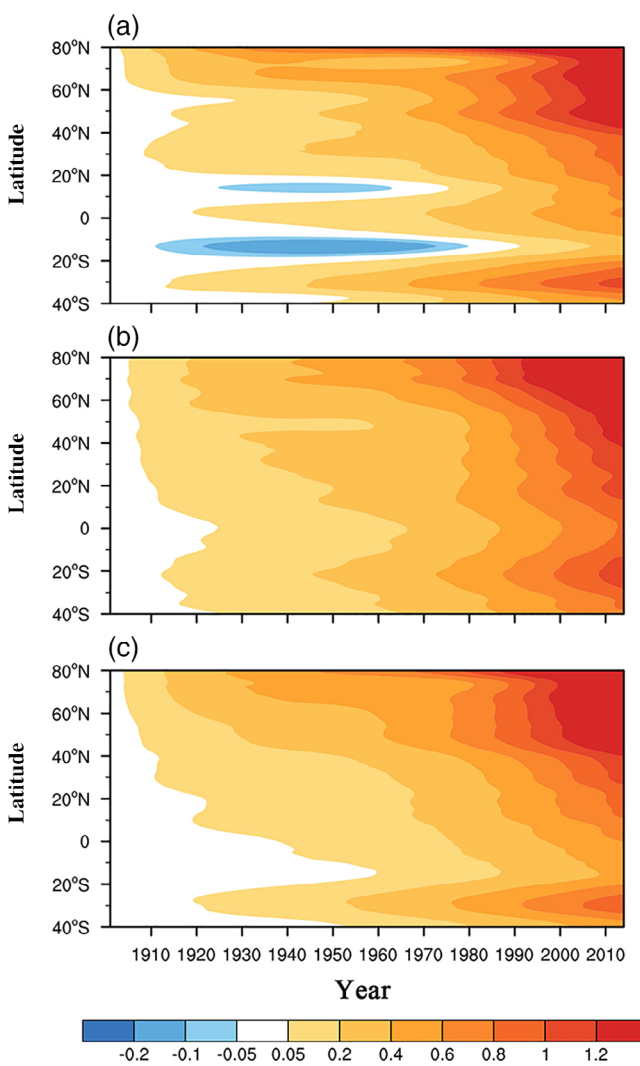


FIGURE 4 1901–2014 the zonal average evolution of ST of SAT in (a) CRU, (b) CMIP6-EM, and (c) CMIP6-EM_{cor} relative to 1901 [Colour figure can be viewed at wileyonlinelibrary.com]

CMIP6-EM_{cor} captured the warming centres in the middle latitudes of the Northern Hemisphere well, and at the same time reduced the overestimation of warming trends in low-latitude regions in Africa, South America, and Oceania by CMIP6-EM.

The change of the ST relative to 1901 in CRU, CMIP6-EM and CMIP6-EM_{cor} were zonally averaged and smoothed at nine points (Figure 4). It was found that the evolution of ST in CMIP6-EM mainly followed a zonal distribution. The maximum warming centres are mainly located in the high latitudes of the Northern Hemisphere and the regions of 20°–30°S. The CMIP6-EM simulation is overestimated overall. The CMIP6-EM_{cor} shows that warming first appeared in high latitudes in the Northern Hemisphere, but the largest warming centre in the Northern Hemisphere was ultimately located in middle latitudes, and the largest warming centre in the Southern

Hemisphere was located at 30°–35°S, which is more consistent with the results of CRU. After calculation, it is found that the ACC of the CMIP6-EM_{cor} and CRU is 0.91, which is an increase of 25% compared to the CMIP6-EM. Apparently, our confidence in the models' simulation of ST of SAT will be strengthened.

In summary, we find that (a) the model has high simulation skills for ST and (b) the result of the CMIP6-EM_{cor} is greatly improved in the simulation skills of ST. Therefore, we apply this correction method to the model's simulation in future scenarios. Furthermore, we evaluate models' simulation skill about secular trends in land surface air temperature, rather than the mean state. The purpose is that for the climate factor of temperature, although its mean state can present the overall spatial distribution and centre of spatial maximum of current global land surface temperatures, we tend to pay more attention to its secular trend, because the magnitude and rate of the change of global temperature often affect the global precipitation distribution pattern, which will further have a huge impact on climate change, including the overall ecosystem.

3.3 | Evolution of future temperature

We select eight models with high simulating skills for ST in historical periods (GISS-E2-1-H and MCM-UA-1-0 do not have monthly average temperature data under future scenarios) and calculate model ensemble mean in the Shared Socioeconomic Pathway 245 (SSP245) scenario and the Shared Socioeconomic Pathway 585 (SSP585) scenario, extend the correction method to the future to correct the model data year by year, obtain the corrected model sequence (CMIP6-EM₂₄₅ and CMIP6-EM₂₄₅), respectively.

Under the SSP245 scenario, the evolution of ST in CMIP6-EM₂₄₅ in Figure 5 shows an upward trend. Warming first appeared in northwest and east North America and eastern Europe, and then the warming spread mainly along these three central regions. By 2050, more than 32.8% of the world's regions will have a warming trend of more than 1.5°C compared to 2015, while the temperature rise in northwest North America and eastern Europe has reached more than 2.0°C, and then the trend of temperature increase will be further strengthened. By 2060, more than half of the world's regions will have a temperature rise of 1.5°C and above, and then rise of the temperature has slowed down. As of the end of this century, the global warming trend exceeds 1.5°C in more than 75.0% of the global land regions. At the same time, the warming in areas exceeding 2.0°C reaches 60.0%, and some high-latitude regions in the Northern Hemisphere have warmed up to 3.6°C or more.

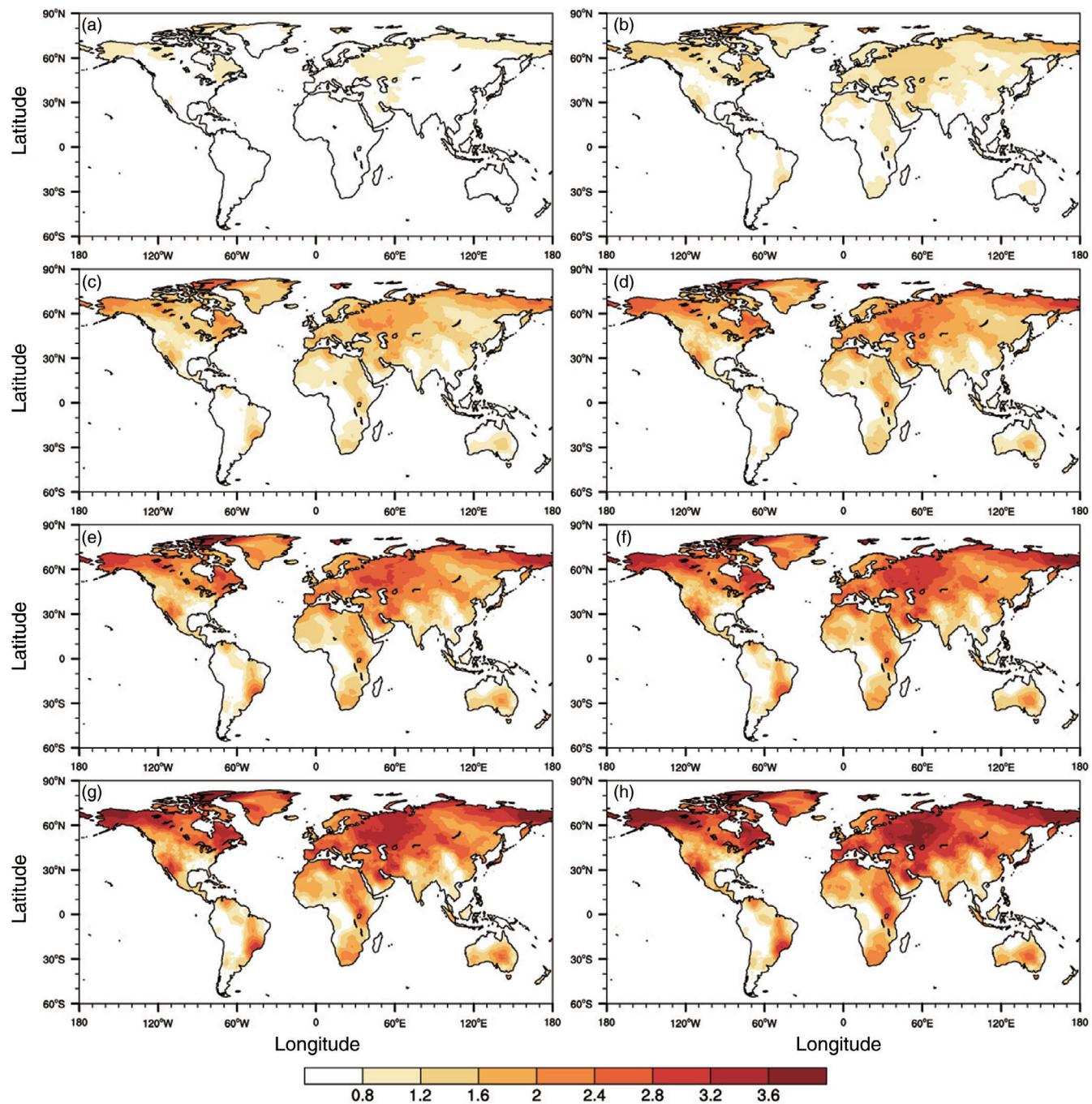


FIGURE 5 The evolution of ST of SAT of CMIP6-EM₂₄₅ in (a) 2030, (b) 2040, (c) 2050, (d) 2060, (e) 2070, (f) 2080, (g) 2090, (h) 2099 relative to 2015 under SSP245 scenario [Colour figure can be viewed at wileyonlinelibrary.com]

It is not difficult to see from Figure 5 that after 2060, the trend evolution of SAT relative to 2015 is slower than that before 2060, which indicates that there are also temporal and spatial changes in the warming rate under the SSP245 scenario. From this, we define the warming rate as the slope of the trend component obtained by EEMD, that is, the temporal derivatives of the ST of SAT. For example, the warming

rate at 1910 is expressed as (EEMD trend at 1911–1909)/2. Under the SSP245 scenario, the warming rate of ST in CMIP6-EM₂₄₅ shows a downward trend (Figure 6). The three large value centres of the initial warming rate basically coincide with the large value centre of the evolution of ST, and they will basically remain at 0.45°C/10 year before 2050, and after 2050, the decrease in the rate of trend evolution is very

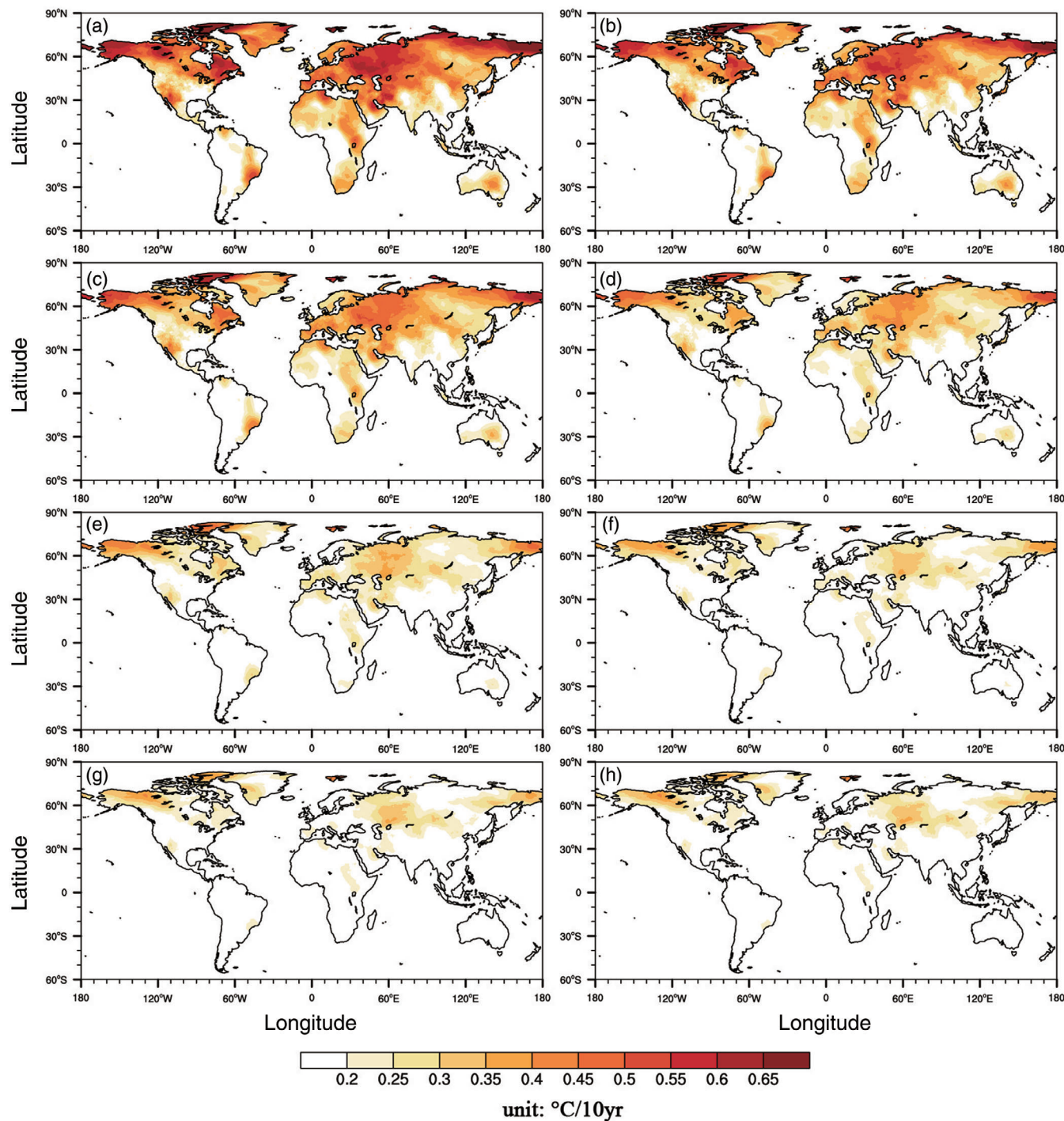


FIGURE 6 The warming rate of ST of SAT of CMIP6-EM₂₄₅ in (a) 2030, (b) 2040, (c) 2050, (d) 2060, (e) 2070, (f) 2080, (g) 2090, (h) 2098 relative to 2015 under SSP245 scenario [Colour figure can be viewed at wileyonlinelibrary.com]

obvious, which is related to the setting of the SSP245 scenario. Under this scenario, the use of renewable energy and the use of fossil fuels continue to decrease, as well as the impact of increased forest area on the increase in carbon storage, resulting in a significant reduction in greenhouse gas emissions (Thomson *et al.*, 2011; Meinshausen *et al.*, 2020).

The evolution of ST under the SSP585 scenario (Figure 7) is similar to the SSP245 scenario (Figure 5), and the initial warming area basically overlaps with the SSP245 scenario, but the magnitude is different. By 2050, 61.0% of the world's regions will have warmed up to 1.5°C, which is nearly twice that under the SSP245 scenario. By the end of this century, the area with temperature higher than 1.5°C

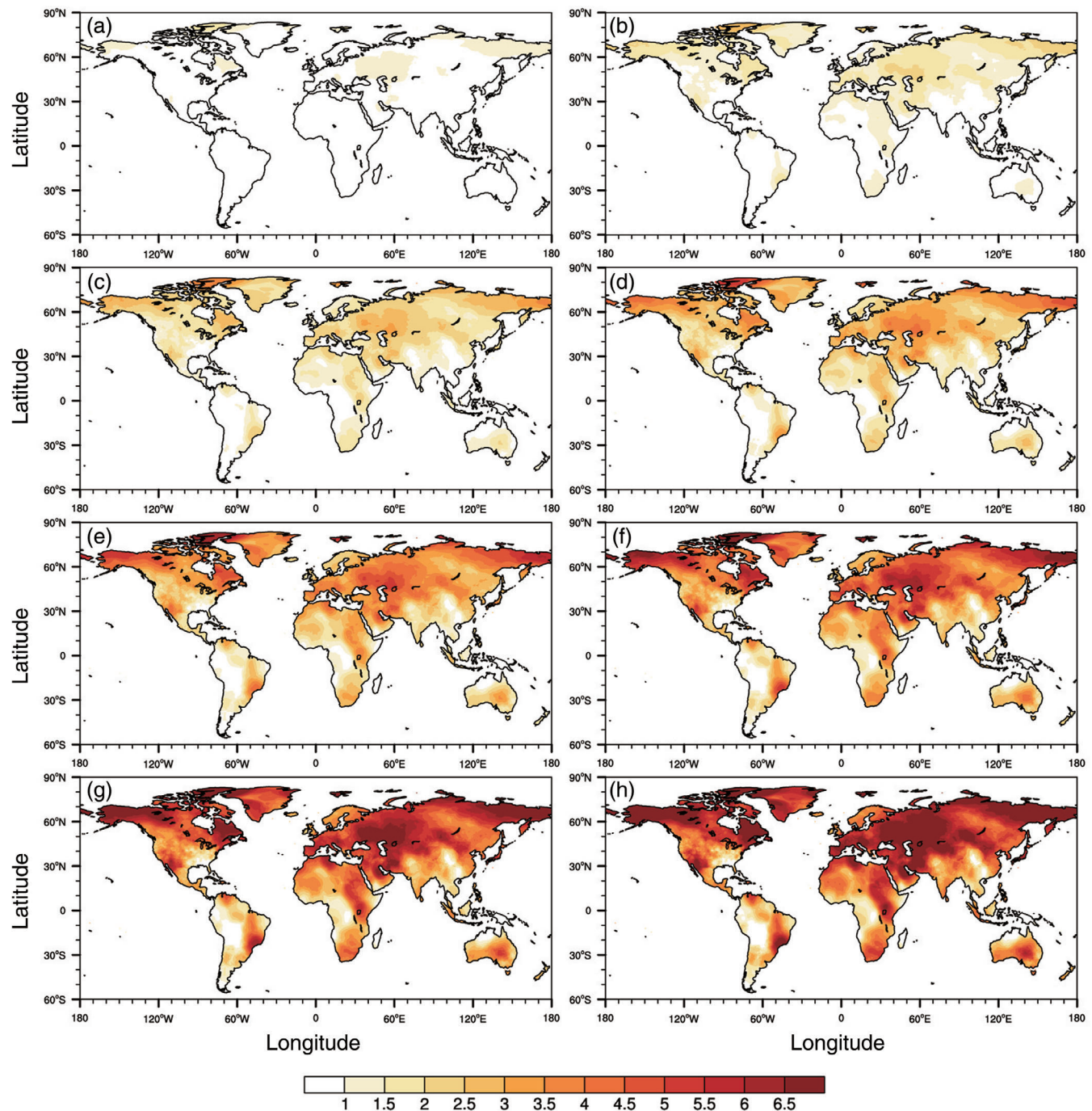


FIGURE 7 The evolution of ST of SAT of CMIP6-EM₅₈₅ in (a) 2030, (b) 2040, (c) 2050, (d) 2060, (e) 2070, (f) 2080, (g) 2090, (h) 2099 relative to 2015 under SSP585 scenario [Colour figure can be viewed at wileyonlinelibrary.com]

has exceeded 92.9%, while the area with a temperature higher than 2.0°C has exceeded 88.7%. SSP585 is also the only scenario where the temperature rises above 3.0, 4.0, and 5.0°C by the end of this century, reaching 78.8, 65.0, and 48.9% of global land surface, respectively.

The warming rate of ST under the SSP585 scenario in Figure 8 is different from that in the SSP245 scenario

(Figure 6), and the upward trend is in line with its own setting of a baseline scenario without any climate change policy intervention. Under this scenario, the substantial increase in global population and changes in energy efficiency have led to greater consumption of fossil fuels, and increasing emissions of greenhouse gases, with radiative forcing reaching $8.5 \text{ W}\cdot\text{m}^{-2}$ by the end of this

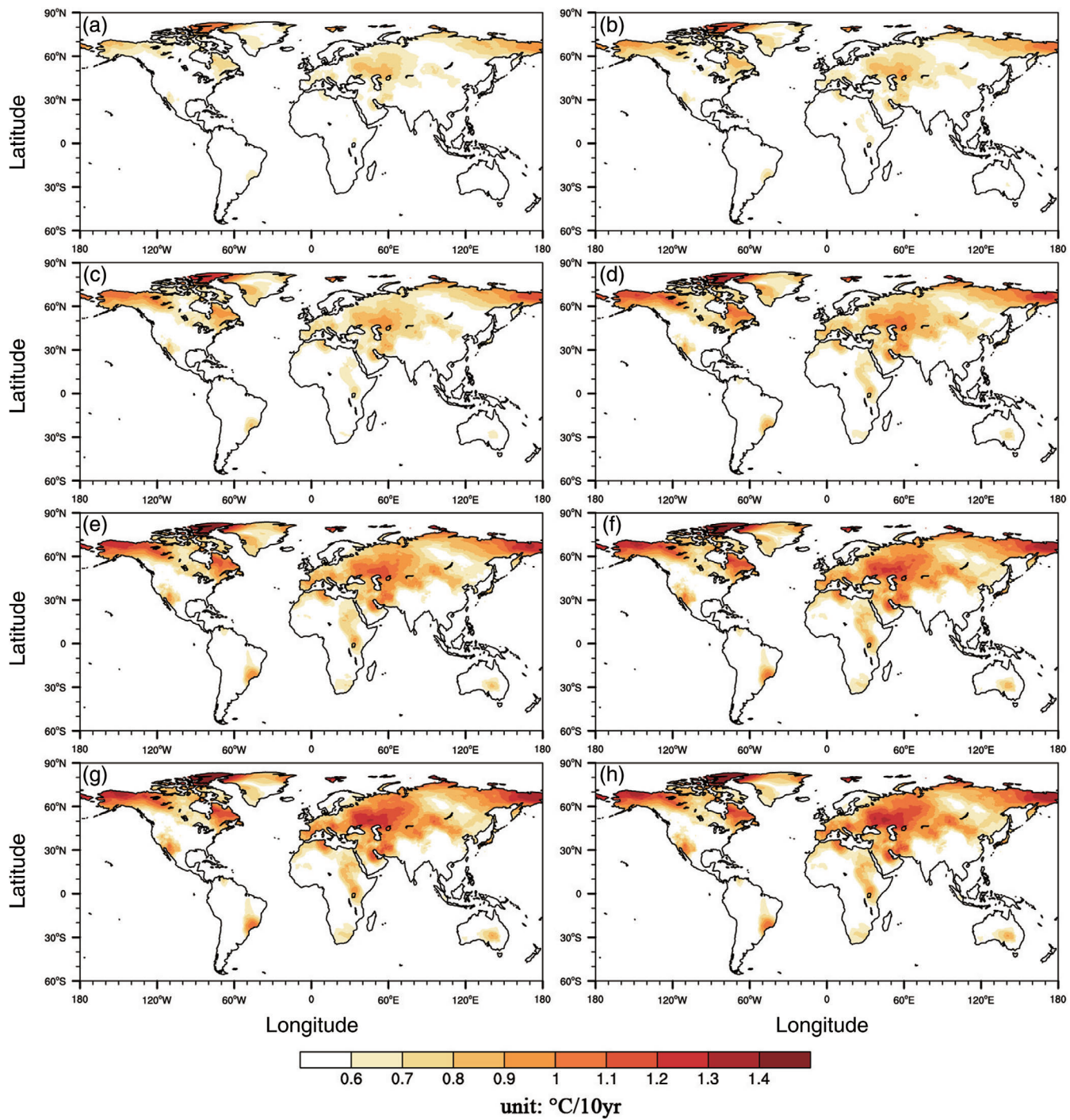
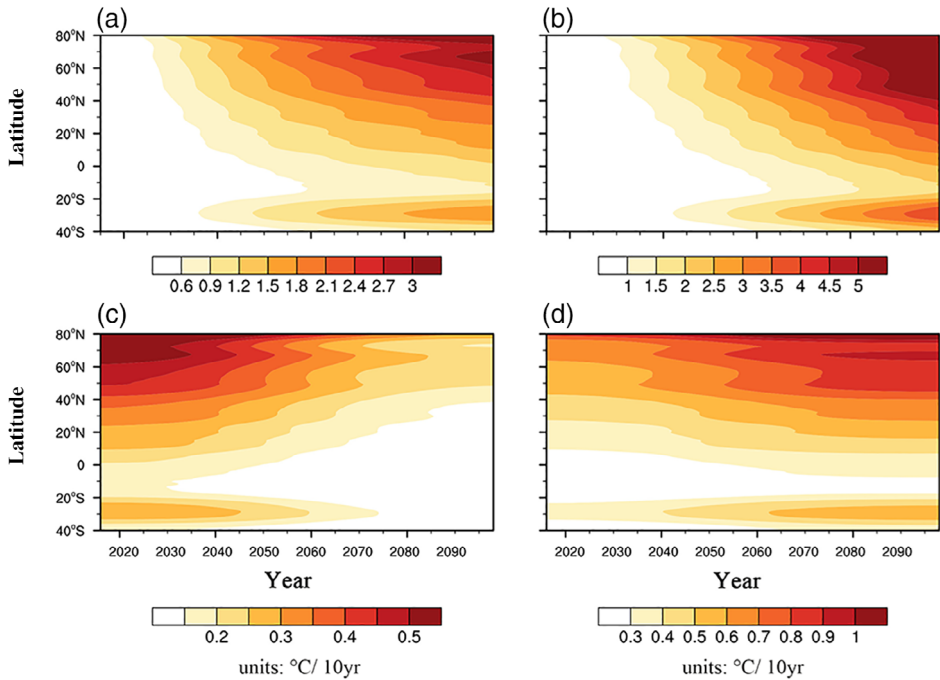


FIGURE 8 The warming rate of ST of SAT of CMIP6-EM₅₈₅ in (a) 2030, (b) 2040, (c) 2050, (d) 2060, (e) 2070, (f) 2080, (g) 2090, (h) 2098 relative to 2015 under SSP585 scenario [Colour figure can be viewed at wileyonlinelibrary.com]

century. The global population will increase dramatically. In order to meet the growing demand for food and energy, the global forest area will decrease and the cultivated land area will increase significantly. This will continue to increase the emission of greenhouse gases in the atmosphere (Riahi *et al.*, 2011; Meinshausen *et al.*, 2020).

It can be found that the zonal average of evolution and warming rate of ST of SAT in Figure 9a,c follows a zonal distribution under SSP245 scenario. The large value centre of temperature evolution (Figure 9a) in the Northern Hemisphere is mainly located in high latitudes, while the Southern Hemisphere is mainly located between 25°S and 35°S.

FIGURE 9 Zonal average of the evolution of ST of SAT in (a) CMIP6-EM₂₄₅, (b) CMIP6-EM₅₈₅ relative to 2015, and zonal average of the warming rate of ST of SAT in (c) CMIP6-EM₂₄₅, (d) CMIP6-EM₅₈₅ relative to 2015. Note that the thresholds of the two colour bars in the same row are different [Colour figure can be viewed at wileyonlinelibrary.com]



The warming rate has shown a clear downward trend over time in Figure 9c. Except for the Arctic, the highest temperature warming rate in the world will appear before 2035, reaching $0.5^{\circ}\text{C}/10$ year, and is basically located in the middle and high latitudes of the Northern Hemisphere. The warming rate of the Southern Hemisphere has always been below $0.3^{\circ}\text{C}/10$ year, and the centre of maximum value lies between 25°S and 35°S .

Under the SSP585 scenario, the large value centre of the temperature evolution in the Northern Hemisphere is mainly located in the middle and high latitudes, while the Southern Hemisphere is mainly located between 25°S and 35°S (Figure 9b), which is consistent with the conclusion of SSP245 scenario. The warming rate shows an obvious upward trend over time in Figure 9d. After 2050, except for 65°N and 70°N , there is no obvious change in the warming rate in the middle and high latitudes of the Northern Hemisphere, basically maintained at $0.8^{\circ}\text{C}/10$ year– $0.9^{\circ}\text{C}/10$ year. Also, the region where warming rate exceeds $0.9^{\circ}\text{C}/10$ year is basically located in the Arctic Circle.

By comparing the evolution characteristics of SAT trend under SSP245 and SSP585 scenarios, it is not difficult to see that the zonal average characteristics of temperature evolution under these two scenarios are basically resemble, but the SSP585 scenario obviously has a larger magnitude (Figure 9a,b). Compared with the warming rate of SAT, a more obvious difference is found. The highlight is that under the SSP245 scenario, the warming rate of SAT shows a downward trend, especially after 2060, the warming rate between 40°S and 40°N is basically less than $0.2^{\circ}\text{C}/10$ year (Figure 9c). This indicates that as of the end of this century,

the rise of temperature will become slower and slower under the SSP245 scenario, which means SAT will only change slightly after reaching a threshold. However, the temperature warming rate in the SSP585 scenario shows an upward trend, which means that the temperature will rise faster and faster as the temperature rises (Figure 9d). So the temperature rise will develop in an uncontrollable direction, and the climate impact brought by the warming will be more serious.

As is in the IPCC AR6 (IPCC, 2021), the changes for 20-year averaging periods in global surface temperature under different future scenarios relative to 1850–1900 were obtained by combining CMIP6 model simulations with observational constraints. It is found that under the SSP245 scenario, the global surface temperature from 2081 to 2100 is in the range of $2.1\text{--}3.5^{\circ}\text{C}$ relative to the pre-industrial period, while the warming range under the SSP585 scenario is $3.3\text{--}5.7^{\circ}\text{C}$. As for our study, we extract land surface air temperature trends by applying the EEMD method and find that more than 90% of the regions where temperature rises above the global land average surface air temperature are located in the Northern Hemisphere under the SSP245 scenario. The regions with higher temperature in the Northern Hemisphere are mainly located in the mid-high latitudes of the Northern Hemisphere, especially in eastern Europe and northwestern North America. As for Southern Hemisphere, only the central and eastern regions of South America in the Southern Hemisphere where temperature rises above 2.9°C . Under the SSP585 scenario, the region where the rise of SAT exceeds 5°C starting from 2080. As of the end

of this century, a lot region located in the Northern Hemisphere has even warmed by more than 6°C .

In addition, this study explores the trend and warming rate of SAT at each grid around the world from a spatial perspective. Compared with other studies on the rise of SAT under various scenarios in the future, it has more pertinent and indicative significance (Zhang *et al.*, 2021; Zhao *et al.*, 2021). Also, amplitude and rate of warming not only affect the frequency of global extreme events (such as the warmest day, warm days, and the warm spell duration indicator, etc.), but also affect the number of people in the world suffering from extreme high-temperature events. Therefore, limiting the future increase in global surface air temperature to a smaller range will have significant implications for global politics, economy, ecology, and so on.

4 | CONCLUSION AND DISCUSSION

In this study, we evaluated the simulation of CMIP6 models of SAT in historical periods. After that, we selected the models with higher simulation skills of ST, calculated CMIP6-EM, and corrected it to obtain a more reliable result. Then, we apply the correction method to the analysis of future scenarios. The main conclusions obtained are as follows:

First, we evaluated the model's skill in simulating SAT in both time and space using four evaluation indices. The evaluation results show that, compared with the reanalysis data, the model's skills for HFC and LFC of SAT are lower, and the modelling skills for secular trend are higher during 1901–2014. This indicates that the model in CMIP6 has a poor ability to capture high-frequency signals.

Second, for the secular trend component, the model and reanalysis data are more temporally consistent than spatially consistent. In order to improve the credibility of the model simulation, we apply a model bias correction method which is significant in the correction effect of low-frequency components. The correction results show that CMIP6-EM_{cor} is closer to the reanalysis data, and the consistency with the reanalysis data improve by 23%.

Finally, we apply the model bias correction method to model simulation under different future scenarios, and analyse the secular trend of corrected model (CMIP6-EM₂₄₅ and CMIP6-EM₅₈₅) find that, the area with a global warming of 1.5°C under the SSP585 scenario will be nearly twice that of the SSP245 scenario by 2050. By the end of this century, the area with a global warming of 2.0°C will reach 60.0/88.7% under the SSP245/SSP585 scenario. In addition, under the SSP245 scenario, the global zonal mean of warming rate shows a downward trend, which means the warming gradually slows down. But under the SSP585

scenario, the warming rate shows an upward trend with time, which indicates that the warming is unstoppable under this scenario.

However, it must be pointed out that there are still many shortcomings in this study. On the one hand, we only discuss the secular trend and warming rate of global land surface air temperature over historical periods and under different future scenarios, ignoring the contribution of the ocean system as an important player in global temperature regulation. On the other hand, the causes of different warming rates under the SSP245 and SSP585 scenarios also need further thinking and research. Nonetheless, our study still provides new directions for studying the spatial patterns and thresholds of future changes in global land surface temperature, and also provides clearer evolutionary results for the magnitude and rate of global warming.

ACKNOWLEDGEMENTS

The authors acknowledge the WCRP Working Group on Coupled Modelling, which is responsible for CMIP, and the climate modelling groups for producing and making available their model outputs. All data are available at <https://esgf-node.llnl.gov/search/cmip6/>. The CRU temperature data were acquired from <https://crudata.uea.ac.uk/cru/data/hrg/>. This work was jointly supported by the National Key Research and Development Program (2017YFC1502305, 2019YFA0607104), National Natural Science Foundation of China (41875083, 41775069, 41975076, 42075029, 41705047, 42075017).

CONFLICT OF INTEREST

The authors declare no potential conflict of interest.

AUTHOR CONTRIBUTIONS

Wen Wu: Data curation; formal analysis; investigation; visualization; writing – original draft. **Fei Ji:** Conceptualization; funding acquisition; writing – review and editing. **Shujuan Hu:** Funding acquisition; writing – review & editing. **Yongli He:** Writing – review and editing. **Yun Wei:** Methodology. **Zhenhao Xu:** Methodology; visualization. **Haipeng Yu:** Methodology.

ORCID

Fei Ji  <https://orcid.org/0000-0002-7985-1558>

Shujuan Hu  <https://orcid.org/0000-0003-1756-434X>

Yun Wei  <https://orcid.org/0000-0002-2965-1881>

REFERENCES

- Bowman, K.W., Cressie, N., Qu, X. and Hall, A. (2018) A hierarchical statistical framework for emergent constraints: application to snow-albedo feedback. *Geophysical Research Letters*, 45, 13050–13059. <https://doi.org/10.1029/2018GL080082>.

- Brient, F. (2020) Reducing uncertainties in climate projections with emergent constraints: concepts, examples and prospects. *Advances in Atmospheric Sciences*, 37, 1–15. <https://doi.org/10.1007/s00376-019-9140-8>.
- Caldwell, p.M., Zelinka, M.D. and Klein, S.A. (2018) Evaluating emergent constraints on equilibrium climate sensitivity. *Journal of Climate*, 31, 3921–3942.
- Chen, H. and Sun, J. (2015) Assessing model performance of climate extremes in China: an intercomparison between CMIP5 and CMIP3. *Climatic Change*, 129, 197–211. <https://doi.org/10.1007/s10584-014-1319-5>.
- Chen, H., Sun, J., Lin, W. and Xu, H. (2020a) Comparison of CMIP6 and CMIP5 models in simulating climate extremes. *Science Bulletin*, 65, 1415–1418. <https://doi.org/10.1016/j.scib.2020.05.015>.
- Chen, X., Zhang, X., Church, J., Watson, C., King, M., Monselesan, D., Legresy, B. and Harig, C. (2017) The increasing rate of global mean sea-level rise during 1993–2014. *Nature Climate Change*, 7, 492–495. <https://doi.org/10.1038/nclimate3325>.
- Chen, X., Zhou, T., Wu, P., Guo, Z. and Wang, M. (2020b) Emergent constraints on future projections of the western North Pacific subtropical high. *Nature Communications*, 11, 2802. <https://doi.org/10.1038/s41467-020-16631-9>.
- Choi, J., Lu, J., Son, S.-W., Frierson, D.M.W. and Yoon, J.-H. (2016) Uncertainty in future projections of the North Pacific subtropical high and its implication for California winter precipitation change. *Journal of Geophysical Research: Atmospheres*, 121, 795–806. <https://doi.org/10.1002/2015JD023858>.
- Coppola, E., Nogherotto, R., Ciarlò, J.M., Giorgi, F., van Meijgaard, E., Kadygrov, N., Iles, C., Corre, L., Sandstad, M., Somot, S., Nabat, P., Vautard, R., Levavasseur, G., Schwingshakl, C., Sillmann, J., Kjellstrom, E., Nikulin, G., Aalbers, E., Lenderink, G., Christensen, O., Boberg, F., Sorland, S., Demory, M., Bulow, K. and Teichmann, C., Warrach-Sagi, K. and Wulfmeyer, V. (2021) Assessment of the European climate projections as simulated by the large EURO-CORDEX regional and global climate model ensemble. *Journal of Geophysical Research: Atmospheres*, 126, e2019JD032356. <https://doi.org/10.1029/2019JD032356>.
- Eyring, V., Bony, S., Meehl, G.A., Senior, C.A., Stevens, B., Stouffer, R.J. and Taylor, K.E. (2016) Overview of the coupled model intercomparison project phase 6 (CMIP6) experimental design and organization. *Geoscientific Model Development*, 9, 1937–1958. <https://doi.org/10.5194/gmd-9-1937-2016>.
- Ferrero, B., Tonelli, M., Marcello, F. and Wainer, I. (2021) Long-term regional dynamic sea level changes from CMIP6 projections. *Advances in Atmospheric Sciences*, 38, 157–167. <https://doi.org/10.1007/s00376-020-0178-4>.
- Gu, L., Chen, J., Yin, J., Xu, C.-Y. and Zhou, J. (2020) Responses of precipitation and runoff to climate warming and implications for future drought changes in China. *Earth's Futures*, 8, e2020EF001718. <https://doi.org/10.1029/2020EF001718>.
- Hall, A., Cox, P., Huntingford, C. and Klein, S. (2019) Progressing emergent constraints on future climate change. *Nature Climate Change*, 9, 269–278. <https://doi.org/10.1038/s41558-019-0436-6>.
- Harris, I., Osborn, T.J., Jones, P. and Lister, D. (2020) Version 4 of the CRU TS monthly high-resolution gridded multivariate climate dataset. *Scientific Data*, 7, 109. <https://doi.org/10.1038/s41597-020-0453-3>.
- Huang, J., Yu, H., Dai, A., Wei, Y. and Kang, L. (2017) Drylands face potential threat under 2°C global warming target. *Nature Climate Change*, 7, 417–422. <https://doi.org/10.1038/nclimate3275>.
- Huang, J., Yu, H., Guan, X., Wang, G. and Guo, R. (2016) Accelerated dryland expansion under climate change. *Nature Climate Change*, 6, 166–171. <https://doi.org/10.1038/nclimate2837>.
- Huang, N.E., Shen, Z., Long, S.R., Wu, M.C., Shih, H.H., Zheng, Q., Yen, N. C., Tung, C.C. and Liu, H.H. (1998) The empirical mode decomposition and the Hilbert spectrum for nonlinear and non-stationary time series analysis. *Proceedings of the Royal Society of London. Series A, Mathematical and Physical Sciences*, 454, 903–995. <https://doi.org/10.1098/rspa.1998.0193>.
- Huang, N.E. and Wu, Z. (2008) A review on Hilbert-Huang transform: method and its applications to geophysical studies. *Reviews of Geophysics*, 46, RG2006. <https://doi.org/10.1029/2007RG000228>.
- IPCC. (2021) Summary for policymakers. In: Masson-Delmotte, V., Zhai, P., Pirani, A., Connors, S.L., Péan, C., Berger, S., Caud, N., Chen, Y., Goldfarb, L., Gomis, M.I., Huang, M., Leitzell, K., Lonnoy, E., Matthews, J.B.R., Maycock, T.K., Waterfield, T., Yelekçi, O., Yu, R. and Zhou, B. (Eds.) *Climate Change 2021: The Physical Science Basis. Contribution of Working Group I to the Sixth Assessment Report of the Intergovernmental Panel on Climate Change*. Cambridge: Cambridge University Press. (in press).
- IPCC. (2022) Global Warming of 1.5°C: IPCC Special Report on impacts of global warming of 1.5°C above pre-industrial levels in context of strengthening response to climate change, sustainable development, and efforts to eradicate poverty. Cambridge, England: Cambridge University Press.
- Ji, F., Wu, Z., Huang, J. and Chassignet, E.P. (2014) Evolution of land surface air temperature trend. *Nature Climate Change*, 4, 462–466. <https://doi.org/10.1038/nclimate2223>.
- Jiang, J., Zhou, T., Chen, X. and Zhang, L. (2020) Future changes in precipitation over Central Asia based on CMIP6 projections. *Environmental Research Letters*, 15, 054009. <https://doi.org/10.1088/1748-9326/ab7d03>.
- Kennedy, J., Blunden, J., Alvar-Beltran, J. and Kappelle, M. (2021) *The State of the Global Climate 2020*. Geneva: WMO.
- Klein, S.A. and Hall, A. (2015) Emergent constraints for cloud feedbacks. *Current Climate Change Reports*, 1, 276–287. <https://doi.org/10.1007/s40641-015-0027-1>.
- Kodra, E., Bhatia, U., Chatterjee, S., Chen, S. and Ganguly, A.R. (2020) Physics-guided probabilistic modeling of extreme precipitation under climate change. *Scientific Reports*, 10, 10299. <https://doi.org/10.1038/s41598-020-67088-1>.
- Krinner, G., Kharin, V., Roehrig, R., Scinocca, J. and Codron, F. (2020) Historically-based run-time bias corrections substantially improve model projections of 100 years of future climate change. *Communications Earth & Environment*, 1, 29. <https://doi.org/10.1038/s43247-020-00035-0>.
- Kumar, D., Kodra, E. and Ganguly, A.R. (2014) Regional and seasonal intercomparison of CMIP3 and CMIP5 climate model ensembles for temperature and precipitation. *Climate Dynamics*, 43, 2491–2581. <https://doi.org/10.1007/s00382-014-2070-3>.
- Kwiatkowski, L., Bopp, L., Aumont, O., Caias, P., Cox, p.M., Laufkötter, C., Li, Y. and Séférian, R. (2017) Emergent constraints on projections of declining primary production in the tropical oceans. *Nature Climate Change*, 7, 355–358. <https://doi.org/10.1038/nclimate3265>.
- Li, D., Zhou, T., Zou, L., Zhang, W. and Zhang, L. (2018) Extreme high-temperature events over East Asia in 1.5°C and 2°C

- warmer futures: analysis of NCAR CESM low-warming experiments. *Geophysical Research Letters*, 45, 1541–1550. <https://doi.org/10.1002/2017GL076753>.
- Li, G., Xie, S., He, C. and Chen, Z. (2017) Western Pacific emergent constraint lowers projected increase in Indian summer monsoon rainfall. *Nature Climate Change*, 7, 708–712. <https://doi.org/10.1038/nclimate3387>.
- Liu, J., Xu, H. and Deng, J. (2018) Projections of East Asian summer monsoon change at global warming of 1.5 and 2°C. *Earth System Dynamics*, 9, 427–439. <https://doi.org/10.5194/esd-9-427-2018>.
- Liu, Y., Chen, J., Pan, T., Liu, Y., Zhang, Y., Ge, Q., Ciais, P. and Penuelas, J. (2020) Global socioeconomic risk of precipitation extremes under climate change. *Earth's Futures*, 8, e2019EF001331. <https://doi.org/10.1029/2019EF001331>.
- Long, S.M., Hu, K.M., Li, G., Huang, G. and Qu, X. (2021) Surface temperature changes projected by FGOALS models under low warming scenarios in CMIP5 and CMIP6. *Advances in Atmospheric Sciences*, 38, 203–220. <https://doi.org/10.1007/s00376-020-0177-5>.
- Lu, J.H. (2020) Constraining the emergent constraints. *Advances in Atmospheric Sciences*, 37, 16–17. <https://doi.org/10.1007/s00376-019-9205-8>.
- Ma, J. and Xie, S. (2013) Regional patterns of sea surface temperature change: a source of uncertainty in future projections of precipitation and atmospheric circulation. *Journal of Climate*, 26, 2482–2501. <https://doi.org/10.1175/JCLI-D-12-00283.1>.
- Maraun, D., Shepherd, T.G., Widmann, M., Zappa, G., Walton, D., Gutiérrez, J.M., Hagemann, S., Richter, I., Soares, p.M.M., Hall, A. and Mearns, L.O. (2017) Towards process-informed bias correction of climate change simulations. *Nature Climate Change*, 7, 664–773. <https://doi.org/10.1038/nclimate3418>.
- Meinshausen, M., Nicholls, Z.R.J., Lewis, J., Gidden, M.J., Vogel, E., Freund, M., Beyerle, U., Gessner, C., Nauels, A., Bauer, N., Canadell, J.G., Daniel, J.S., John, A., Krummel, p.B., Luderer, G., Meinshausen, N., Montzka, S.A., Rayner, p.J., Reimann, S., Smith, S.J., van den Berg, M., Velders, G.J.M., Vollmer, M.K. and Wang, R.H.J. (2020) The shared socio-economic pathway (SSP) greenhouse gas concentrations and their extensions to 2500. *Geoscientific Model Development*, 13, 3571–3605. <https://doi.org/10.5194/gmd-13-3571-2020>.
- Mishra, V., Bhatia, U. and Tiwari, A.D. (2020) Bias-corrected climate projections for South Asia from Coupled Model Intercomparison Project-6. *Scientific Data*, 7, 338. <https://doi.org/10.1038/s41597-020-00681-1>.
- Moss, R.H., Edmonds, J.A., Hibbard, K.A., Manning, M.R., Rose, S. K., van Vuuren, D.P., Carter, T.R., Emori, S., Kainuma, M., Kram, T., Meehl, G.A., Mitchell, J.F.B., Nakicenovic, N., Riahi, K., Smith, S.J., Stouffer, R.J., Thomson, A.M., Weyant, J. P. and Wilbanks, T.J. (2010) The next generation of scenarios for climate change research and assessment. *Nature*, 463, 747–756. <https://doi.org/10.1038/nature08823>.
- Piani, C., Haerter, J.O. and Coppola, E. (2010) Statistical bias correction for daily precipitation in regional climate models over Europe. *Theoretical and Applied Climatology*, 99, 187–192. <https://doi.org/10.1007/s00704-009-0134-9>.
- Qi, Y., Qian, C. and Yan, Z. (2017) An alternative multi-model ensemble mean approach for near-term projection. *International Journal of Climatology*, 37, 109–122. <https://doi.org/10.1002/joc.4690>.
- Qian, C., Wu, Z., Fu, C. and Zhou, T. (2010) On multi-timescale variability of temperature in China in modulated annual cycle reference frame. *Advances in Atmospheric Sciences*, 27, 1169–1182. <https://doi.org/10.1007/s00376-009-9121-4>.
- Qin, p.H., Xie, Z.H., Zou, J., Liu, S. and Chen, S. (2021) Future precipitation extremes in China under climate change and their physical quantification based on a regional climate model and CMIP5 model simulations. *Advances in Atmospheric Sciences*, 38, 460–479. <https://doi.org/10.1007/s00376-020-0141-4>.
- Rao, J., Liu, S. and Chen, Y. (2021) Northern Hemisphere sudden stratospheric warming and its downward impact in four Chinese CMIP6 models. *Advances in Atmospheric Sciences*, 38, 187–202. <https://doi.org/10.1007/s00376-020-0250-0>.
- Riahi, K., Rao, S., Krey, V., Cho, C., Chirkov, V., Fischer, G., Kindermann, G., Nakicenovic, N. and Rafaj, P. (2011) RCP 8.5—a scenario of comparatively high greenhouse gas emissions. *Climatic Change*, 109, 33–57. <https://doi.org/10.1007/s10584-011-0149-y>.
- Shen, C., Duan, Q., Miao, C., Xing, C., Fan, X., Wu, Y. and Han, J. (2020) Bias correction and ensemble projections of temperature changes over ten subregions in CORDEX East Asia. *Advances in Atmospheric Sciences*, 37, 1191–1210. <https://doi.org/10.1007/s00376-020-0026-6>.
- Stocker, T., Qin, D. and Plattner, G. (2014) *Climate Change 2013: The Physical Science Basis*. Cambridge, England: Cambridge University Press. <https://doi.org/10.1017/CBO9781107415324>.
- Taylor, K.E., Stouffer, R.J. and Meehl, G.A. (2012) An overview of CMIP5 and the experiment design. *Bulletin of the American Meteorological Society*, 93, 485–498.
- Terink, W., Hurkmans, R.T.W.L., Torfs, p.J.J.F. and Uijlenhoet, R. (2010) Evaluation of a bias correction method applied to down-scaled precipitation and temperature reanalysis data for the Rhine basin. *Hydrology and Earth System Sciences*, 14, 687–703. <https://doi.org/10.5194/hess-14-687-2010>.
- Thaler, V., Loikith, p.C., Mechoso, C.R. and Pampuch, L.A. (2021) A multivariate assessment of climate change projections over South America using the fifth phase of the Coupled Model Intercomparison project. *International Journal of Climatology*, 41, 4265–4282. <https://doi.org/10.1002/joc.7072>.
- Thomson, A.M., Calvin, K.V., Smith, S.J., Kyle, G.P., Volke, A., Patel, P., Delgado-Arias, S., Bond-Lamberty, B., Wise, M.A., Clarke, L.E. and Edmonds, J.A. (2011) RCP4.5: a pathway for stabilization of radiative forcing by 2100. *Climatic Change*, 109, 77–94. <https://doi.org/10.1007/s10584-011-0151-4>.
- Tokarska, K.B., Stolpe, M.B., Sippel, S., Fischer, E.M., Smith, C.J., Lehner, F. and Knutti, R. (2020) Past warming trend constrains future warming in CMIP6 models. *Science Advances*, 6, eaaz9549. <https://doi.org/10.1126/sciadv.aaz9549>.
- UNFCCC. (2015) *Adoption of the Paris Agreement*. United Nations.
- Wei, Y., Yu, H., Huang, J., Liu, X. and Zhou, J. (2021) Improving China's summer precipitation prediction in 2020 by observational constrained bias correction. *Theoretical and Applied Climatology*, 145, 1317–1331. <https://doi.org/10.1007/s00704-021-03693-y>.
- Wenzel, S., Cox, p.M., Eyring, V. and Friedlingstein, P. (2014) Emergent constraints on climate-carbon cycle feedbacks in the CMIP5 Earth system models. *Journal of Geophysical Research: Biogeosciences*, 119, 794–807. <https://doi.org/10.1002/2013JG002591>.

- Wu, Z. and Huang, N.E. (2009) Ensemble empirical mode decomposition: a noise-assisted data analysis method. *Advances in Adaptive Data Analysis*, 1, 1–41. <https://doi.org/10.1142/S1793536909000047>.
- Wu, Z., Huang, N.E. and Chen, X. (2009) The multi-dimensional ensemble empirical mode decomposition method. *Advances in Adaptive Data Analysis*, 1, 339–372. <https://doi.org/10.1142/S1793536909000187>.
- Xie, Y., Liu, Y. and Huang, J. (2016) Overestimated Arctic warming and underestimated Eurasia mid-latitude warming in CMIP5 simulations. *International Journal of Climatology*, 36, 4475–4487. <https://doi.org/10.1002/joc.4644>.
- Xu, Z., Ji, F., Liu, B., Feng, T., Gao, Y., He, Y. and Chang, F. (2021) Long-term evolution of global sea surface temperature trend. *International Journal of Climatology*, 41, 4494–4508. <https://doi.org/10.1002/joc.7082>.
- Yao, J., Liu, H., Huang, J., Gao, Z., Wang, G., Li, D., Yu, H. and Chen, X. (2020) Accelerated dryland expansion regulates future variability in dryland gross primary production. *Nature Communications*, 11, 1665. <https://doi.org/10.1038/s41467-020-15515-2>.
- Yu, H., Zhang, Q., Wei, Y., Liu, C., Ren, Y., Yue, P. and Zhou, J. (2022) Bias-corrections on aridity index simulations of climate models by observational constraints. *International Journal of Climatology*, 42(2), 889–907. <https://doi.org/10.1002/joc.7279>.
- Zhang, G.W., Zeng, G., Yang, X.Y. and Jiang, Z.H. (2021) Future changes in extreme high temperature over China at 1.5°C–5°C global warming based on CMIP6 simulations. *Advances in Atmospheric Sciences*, 38, 253–267. <https://doi.org/10.1007/s00376-020-0182-8>.
- Zhao, Y., Qian, C., Zhang, W., He, D. and Qi, Y. (2021) Extreme temperature indices in Eurasia in a CMIP6 multi-model ensemble: evaluation and projection. *International Journal of Climatology*, 41, 5368–5385. <https://doi.org/10.1002/joc.7134>.
- Zhu, H., Jiang, Z., Li, J., Li, W., Sun, C. and Li, L. (2020) Does CMIP6 inspire more confidence in simulating climate extremes over China? *Advances in Atmospheric Sciences*, 37, 1119–1132. <https://doi.org/10.1007/s00376-020-9289-1>.

How to cite this article: Wu, W., Ji, F., Hu, S., He, Y., Wei, Y., Xu, Z., & Yu, H. (2022). Future evolution of global land surface air temperature trend based on Coupled Model Intercomparison Project Phase 6 models. *International Journal of Climatology*, 1–17. <https://doi.org/10.1002/joc.7668>